

# A cross-scale characterization of porous rocks altered by flow and dissolution

Xu, Z., and Li, W.

*Department of Civil Engineering, Stony Brook University, Stony Brook, NY, USA*

Kolanti, A. and Sprouter, D.

*Department of Material Science and Chemical Engineering, Stony Brook University, Stony Brook, NY, USA*

Copyright 2024 ARMA, American Rock Mechanics Association

This paper was prepared for presentation at the 58th US Rock Mechanics/Geomechanics Symposium held in Golden, Colorado, USA, 23–26 June 2024. This paper was selected for presentation at the symposium by an ARMA Technical Program Committee based on a technical and critical review of the paper by a minimum of two technical reviewers. The material, as presented, does not necessarily reflect any position of ARMA, its officers, or members. Electronic reproduction, distribution, or storage of any part of this paper for commercial purposes without the written consent of ARMA is prohibited. Permission to reproduce in print is restricted to an abstract of not more than 200 words; illustrations may not be copied. The abstract must contain conspicuous acknowledgement of where and by whom the paper was presented.

**ABSTRACT:** Flow and dissolution induce wormholes in porous rocks, which lead to a substantial increase in both permeability and flow heterogeneity of the rock formation. Wormholes originate from the initial micron-scale pore networks, and gradually transition to more prominent millimeter-scale holes. Wormholes have a crucial impact on the flow and reactions in subsurface technologies, such as critical mineral leaching, CO<sub>2</sub> storage and reservoir stimulation. Understanding how wormholes form from pore networks is crucial for the effectiveness of these subsurface technologies. However, current studies are limited to two separate scales of characterizations: millimeter-scale wormholes and micron-scale pore networks. The transitional region, which bridges these features at the two scales, remains largely unexplored and inadequately characterized. This knowledge gap obscures our understanding of the underpinning physics that governs wormhole formation in porous rocks. In this study, we aim to bridge these two scales of study with multiscale characterization. We create wormholes in porous gypsum specimens through core flood tests. The wormholes are then scanned with low-resolution (26.70 μm) and high-resolution (3.43 μm) X-ray computed tomography (CT). We quantitatively characterize the geometry of the wormholes leading to pore networks regarding their diameters, and quantities. This 3D cross-scale characterization allows for an accurate depiction of the interactions between wormholes and pore networks and provides physical insights into the initiation of wormholes.

## 1 INTRODUCTION

Wormholes are long and finger-like channels resulting from the heterogeneity in flow and dissolution within a porous medium (Szymczak and Ladd, 2009; Li et al., 2022). Wormhole formation is common in many natural and industrial processes, such as enhanced oil production and CO<sub>2</sub> storage (Hoefner and Fogler, 1988; Gouze and Luquot, 2011; Smith et al., 2013; Menke et al., 2015; Wang et al., 2016). Wormholes significantly increase the permeability of the porous media and localize the flow and consequently heat and mass transfer between the fluid and porous media. Understanding how the wormholes emerge and quantifying their impact on the porous media during the subsurface resource exploitation are crucial in the engineering of the aforementioned subsurface systems.

The geometry of a wormhole is usually invisible due to the surrounded rock matrix, much of the research on wormholes rely on X-ray computed tomography (CT) to study

and characterize the millimeter-scale wormholes in porous rocks (Fredd and Fogler, 1998; Gouze et al., 2003; Noiriel, 2015; Deng et al., 2016; Yang et al., 2018). Recently, in-situ X-ray CT has been used to capture the temporal evolution of wormhole formation (Cooper et al., 2023). 3D topological and morphological algorithms have been introduced to quantitatively characterize the millimeter-scale wormholes (Li and Einstein, 2017; Li et al., 2019b, 2022). On the other hand, the pore network, from where the wormholes originate, has been observed using micron-resolution tomographic techniques, for example, synchrotron CT (Blunt et al., 2013; Andrew et al., 2015). The X-ray CT imaging systems is a crucial technique for the three-dimensional characterization of wormholes, but both the scanning resolution and scanning outcomes are constrained by several factors (noise, pixel size), resulting in limited access to either millimeter-scale wormholes or micrometer-scale pore networks (Elkhoury et al., 2019;

Lin et al., 2024). To better understand wormhole initiation and its interaction with the pore network, it is crucial to have cross-scale characterization of the porous rock with wormholes to bridge the features in the two-scales, wormholes and pore networks, which are physically connected after all.

This study builds upon the experiments and quantitative analysis reported by Li et al. (2019b, 2022) to investigate the wormhole formation in a gypsum-water system with cross-scale characterization and 3D topological analysis. The gypsum-water system was used as a representative rock-fluid reactive transport system and core flood tests were carried out with three different flow rates. The wormholes resulting from different flow rates were observed using different resolutions (26.70  $\mu\text{m}$  and 3.43  $\mu\text{m}$ ) with non-destructive X-ray CT scan. Topological and morphological algorithms were developed to process the 3D CT scan data and reconstruct the geometry of wormholes in the specimens at the two scales, which will allow us to understand the transition from wormholes to the pore network.

## 2 MATERIAL AND SPECIMEN PREPARATION

Gypsum is a soluble mineral and rock. The gypsum-water system has been used to investigate gypsum karst geology, or as an analog modeling system for the reactive transport processes in other rock-fluid systems (Daccord, 1987; Johnson, 2008; Lipar et al., 2021; Grodzki and Szymczak, 2019). In this study, The preparation process of gypsum is based on Einstein et al. (1969). A water-to-plaster mass ratio of 0.6 is used to ensure complete hydration and achieve optimal workability. The plaster and water are thoroughly mixed in a mixer for two minutes. Then, the mixture is poured into the mold and subjected to vibration for an additional two minutes to ensure uniformity and minimize the presence of air bubbles within the specimen. After curing the specimen in a 40 °C oven for one day, the gypsum attains sufficient strength to be removed from the mold for further drying. The gypsum is cured at 40 °C for 7 days and cut into cylindrical specimens with 1-inch (2.54 cm) diameter and 2-inch length (5.08 cm) (Fig. 1). The key material properties of the specimens, such as porosity and permeability, were measured, as summarized in Table 1.

The density of the specimen, approximately 1.18 g/cm<sup>3</sup>, is calculated from the measured specimen mass and volume. Considering a specific gravity of 2.32 for the gypsum mineral (Serafeimidis and Anagnostou, 2013), the porosity calculated based on phase relationships ranges from 0.48 to 0.51, which is also in the porosity range of 0.40-0.60

Table 1: Properties of the Six Specimens

Specimen	G1	G2	G3	G4	G5	G6
Flow Rate (mL/min)	0.20	0.20	1.00	1.00	1.80	1.80
Length (cm)	5.05	4.97	5.10	5.05	5.07	5.10
Diameter (cm)	2.55	2.55	2.56	2.55	2.56	2.56
Mass (g)	30.65	30.28	30.91	30.45	30.89	30.05
Density (g/cm <sup>2</sup> )	1.18	1.18	1.17	1.18	1.16	1.18
Porosity	0.488	0.487	0.492	0.491	0.491	0.501
Permeability (mD)	92.80	89.10	74.93	74.88	71.56	77.15

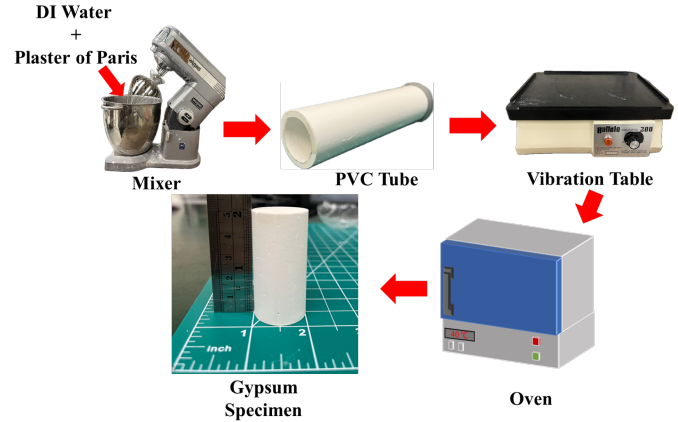


Fig. 1: The gypsum specimen preparation (The mixer was used with a mass ratio of 0.6 water to plaster; PVC was utilized as the mold for the plaster cast; A vibration table was employed to remove internal bubbles; Subsequently, the specimen was cured in an oven at 40 °C for one day to facilitate unmolding, followed by an additional seven days of curing to allow for cutting and polishing).

for gypsum according to Einstein et al. (1969); Daccord (1987); Li et al. (2019b, 2022). The permeability of the specimen is measured based on the initial pressure difference during the core flood test. It is worth mentioning that the presence of air bubbles inside the specimen is inevitable, which is similar to the largest pores, voids, or natural fractures with initial heterogeneity, affecting formation of the wormhole topological structure.

## 3 EXPERIMENTAL SETUP

The experimental study consists of two main parts: core flood tests, and cross-scale characterization, including low-resolution (26.70  $\mu\text{m}$ ) scans of the entire specimens and high-resolution scans (3.43  $\mu\text{m}$ ) for wormhole-pore transition zones.

### 3.1. Core Flood Tests

In each core flood test, a specimen is housed in a triaxial system with a uniform confining stress of 100 psi (690 kPa)(Fig. 2). The specimen is vacuum-saturated with gyp-

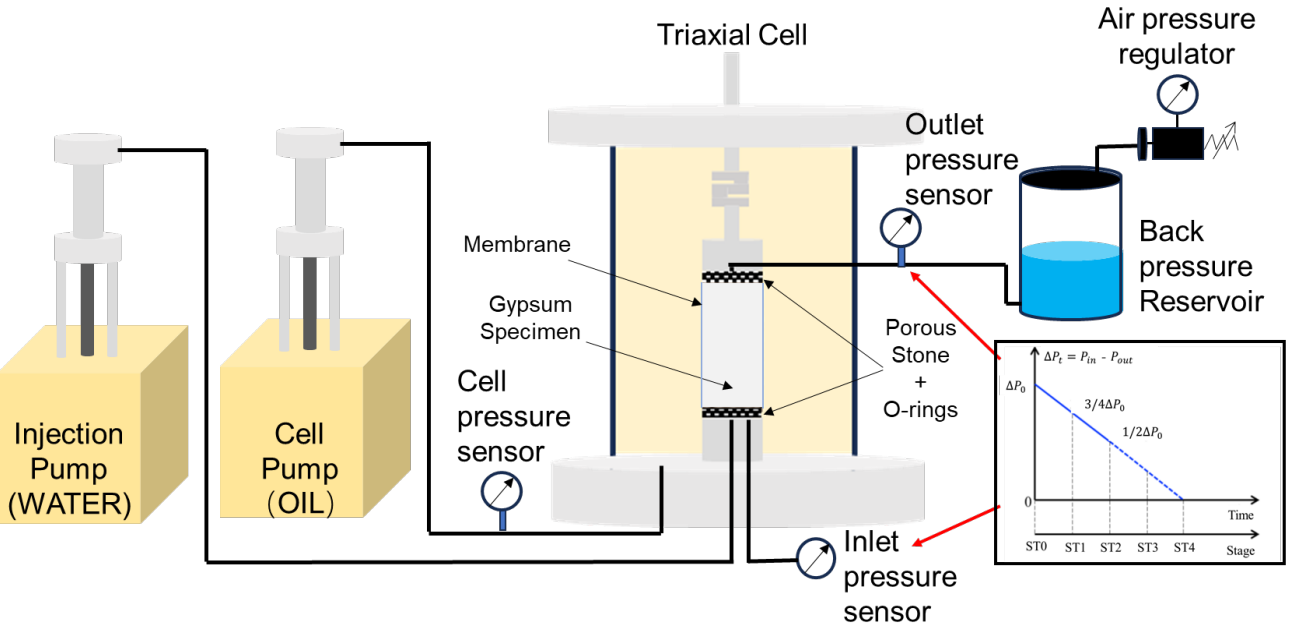


Fig. 2: Diagram of the triaxial setup adapted for core flood tests.

sum solution to ensure single-phase flow and avoid dissolution, and a back pressure of 10 psi (69 kPa) is applied. After the overnight saturation for temperature equilibrium, the distilled water is injected through the specimen. The pressure difference between the inlet and outlet of the specimen is continuously monitored. The core flood test is ended when the pressure difference ( $\Delta P_t$ ) between the inlet and outlet of the specimen reaches half of the initial value ( $P_0$ ). Three flow rates ( $Q$ ) are utilized, with each flow rate tested repeatedly (0.20 mL/min, 1.00 mL/min, 1.80 mL/min). The physical parameters (inlet pressure, outlet pressure, confining pressure, injected volume) are recorded every 3 seconds during each test. After the core flood tests, the specimens are dried at 40 °C for 7 days before the X-ray CT scan.

### 3.2. Low-resolution and high-resolution scans

After the core flood test, the six specimens are first scanned with a 26.70-micron voxel resolution using the X-ray CT scanner, ZEISS Xradia 520 Versa operating at 80 kV and 7 W, and a exposure time of 1.5 s. The specimens are rotated 360 degrees while X-ray radiographs are obtained for 3D reconstruction of the specimens.

Based on the 3D reconstruction from the low-resolution scan, we visualize the wormholes of the 6 specimens and choose the specimen (G5) for the high-resolution scan. G5 has a wormhole tip developed along the center axis of the specimen, which makes it easy to locate in the zoom-in view. The wormhole tip is scanned with a 3.43-micron voxel resolution with non-destructive method. A 4× X-

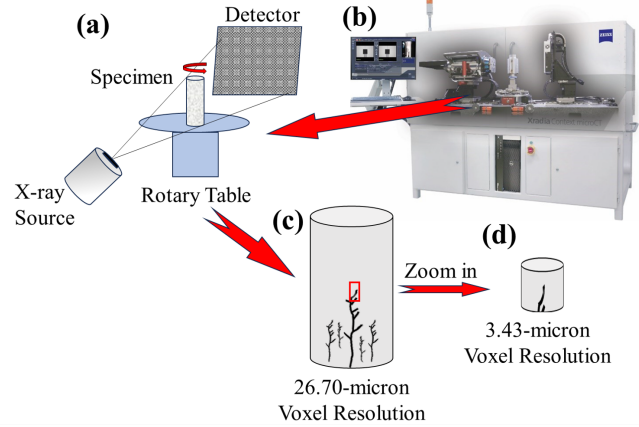


Fig. 3: Diagram of the computed tomography scan: (a) Schematic of the computed tomography scan setup; (b) Internal structure of the ZEISS Xradia 520 Versa; (c) 26.70-micron voxel resolution for whole specimen; (d) 3.43-micron voxel resolution for the transition region.

ray lens is used to boost the magnification to achieve the 3.43-micron voxel resolution. Fig. 3 illustrates the low-resolution and high-resolution scans. Due to the limitation of scanning platform height for all scans, the sample's X-ray radiographs were obtained by vertical stitching. All data for each sample was collected in three separate regions with overlap, and stitched together to maximize scan volume, while maintaining a high resolution.

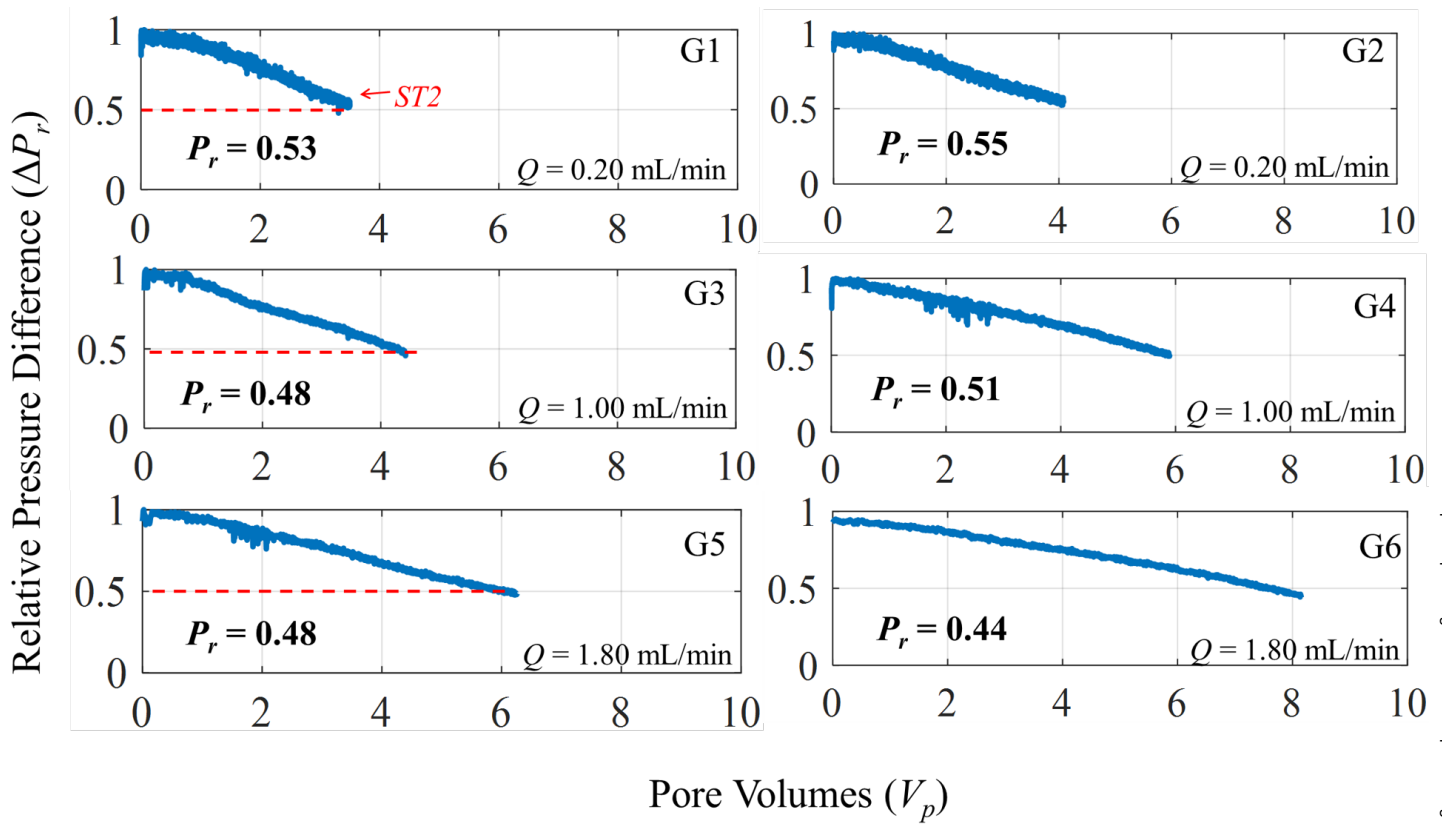


Fig. 4: Relative pressure difference between the inlet and outlet during the core flood tests.

## 4 EXPERIMENTAL RESULTS

### 4.1. Core Flood Test Results

The pressure difference is normalized by its initial value, as the relative pressure differences ( $P_r = \Delta P / \Delta P_0$ ) shown in Fig. 4. The injected pore volume ( $V_p$ ) is calculated for each test as the X axis. It is defined as the injected volume ( $V_{inject} = Q \cdot t$ ) normalized by the initial pore volume of the specimen  $V_{pore}$ ,  $V_p = Q \cdot t / V_{pore}$  ( $Q$  and  $V_{pore}$  are constant in each test). The target relative pressure difference ( $P_r=0.5$ ) and actual  $P_r$  for each core flood test are shown in Fig. 4. The tests are ended very close to the targeted  $P_r$ , except for G6. This test is ended later than planned and results in longer wormholes.

As shown in Fig. 4, the slopes of the curves decrease as the flow rates rise. This trend suggests a positive correlation between the injected flux and the flow rate, which means a larger volume of liquid is needed to reach the target stage under higher flow rates, leading to the formation of more wormholes upon reaching the same target stage. Additionally, wormholes form faster at high flow rates according to the wormhole conceptual model and equation derivation by Daccord et al. (1993); Li et al. (2019b).

### 4.2. Low-resolution Scan of Entire Specimens

#### 4.2.1. 3D wormhole reconstruction

After the CT scan, the image stack for each test are exported, and each image in the stack is the greyscale cross-section of the specimen. Gypsum's image segmentation for the solid phase and air phase is relatively straightforward (Deng et al., 2016). The 3D binary matrix (1 (white) represents void space and 0 (black) represents solid) is used to reconstruct the wormholes (Li et al., 2019a; Li and Juanes, 2023). The software ParaView® was used to produce the 3D rendering of the wormholes with color indicating the wormhole diameter shown in Fig. 5 (Li et al., 2019a).

The wormholes develop from the inlet, and stop roughly in the middle of the specimens, resenting a root-like geometry. There is a major wormhole for each specimen, and more secondary wormholes and more branches are formed with higher flow rate, which is consistent with previously reported results (Fredd and Fogler, 1998; Budek and Szymczak, 2012). It is worth noting that the complexity and number of wormholes are larger at high flow rate, but the diameter of wormholes becomes smaller. According to the research based on Cooper et al. (2023), the shape of wormholes becomes thinner and more tortuous under higher flow rates, and then we verify this result by

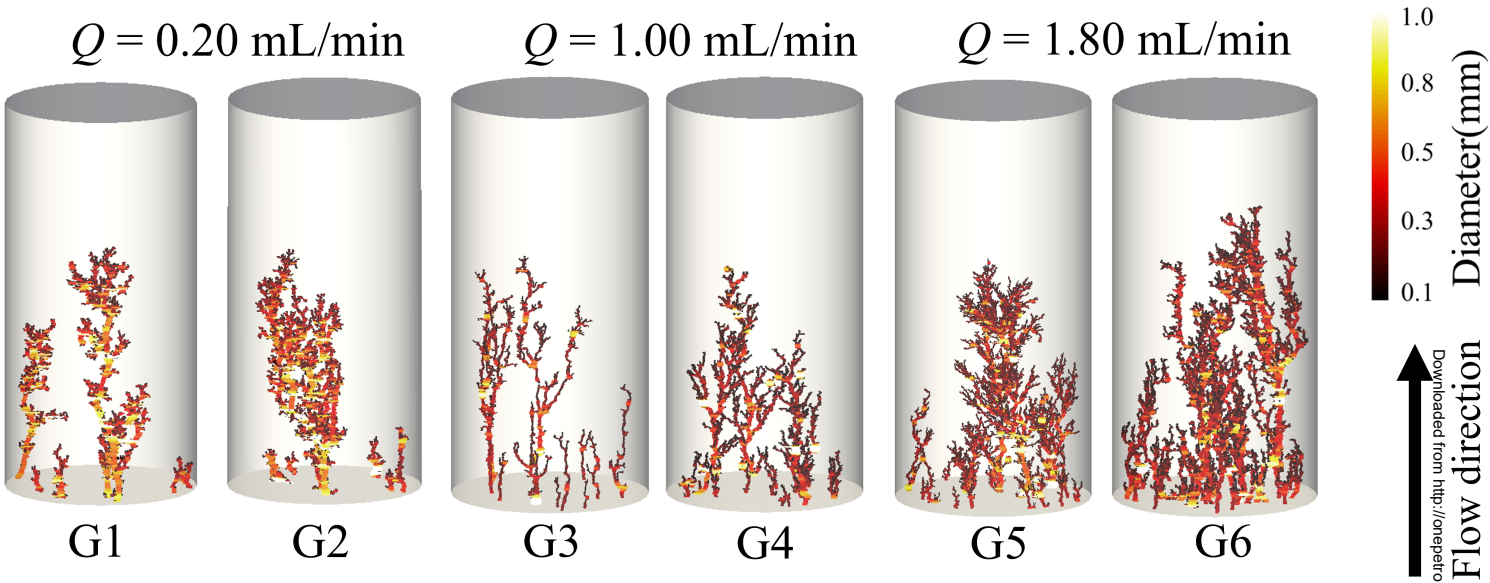


Fig. 5: Three dimensional reconstructions of the wormholes.

quantitative analysis.

#### 4.2.2. Total Area and Number of Wormholes

We quantify the number of conduits (wormholes and branches) ( $N_{cd}$ ) and the total area ( $S_{cd}$ ) of these conduits by analyzing each cross section of a specimen. As the result shown in Fig. 6, the area (total number of conduits) between the abscissa and curve at 1.80 mL/min is about two or three times as many as other flow rates, as fluid is forced into smaller pores, resulting in the flow channels be more highly branched or ramified. Additionally, the  $N_{cd}$  of G6 decreases linearly going upwards of the sample, that means the inlet of the wormholes are larger than the rest of the wormholes. This is caused by the nonuniform dissolution along the wormholes. (Smith et al., 2017, 2013; Wang et al., 2016). But for the G5, instead of following the same trend, the curve has a distinct step-wise change, since the wormhole connects air bubbles as part of the wormhole during the propagation. Larger bubbles lead to abrupt changes in number and area (details will be will be discussed in section 4.3). Most importantly, at a low flow rate (0.20 mL/min) with less number of connections, the total area of the conduit is not much different from the total area of the other two flow rates. This indicates that lower flow rate results in wormholes and branches of large diameter.

#### 4.2.3. Wormhole Diameter Analysis

The probability density of conduit diameters on each cross section of each specimen is plotted in Fig. 7. The diameter of the conduits formed by each flow rate looks similar

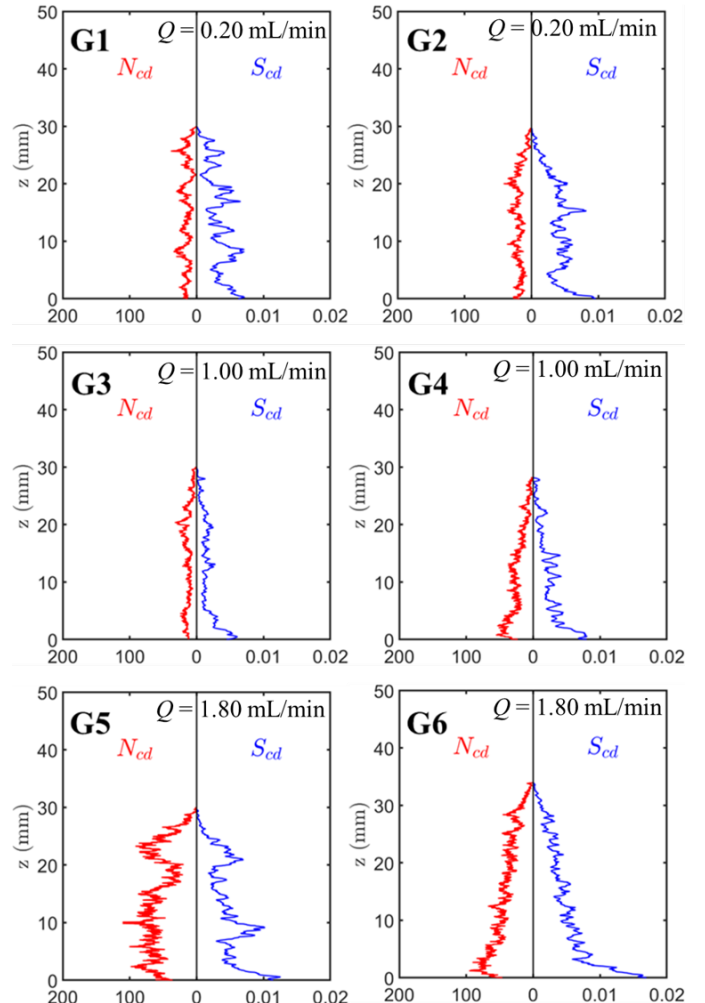


Fig. 6: Number of Wormhole ( $N_{cd}$ ) and normalized total Wormhole area ( $S_{cd}$ ) on each horizontal cross section of each specimen.

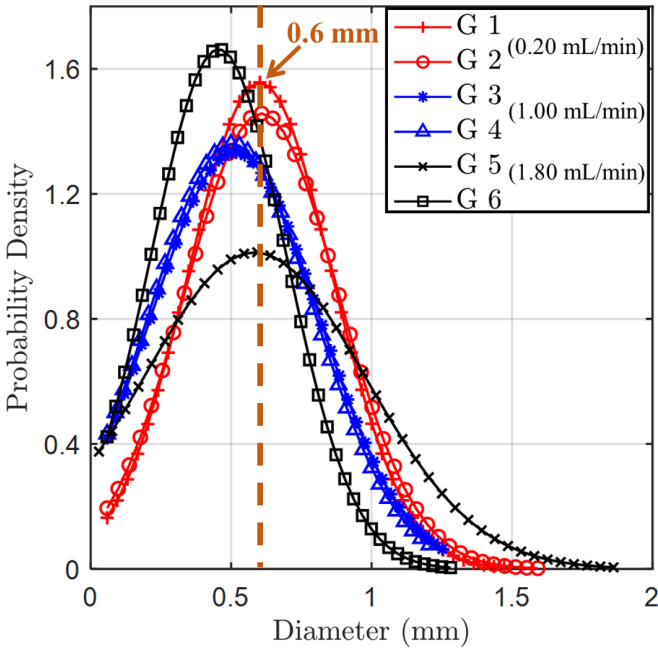


Fig. 7: The probability density of conduits diameter on each cross section of each specimen. The vertical dotted line: the main distribution of conduits diameter at 0.20 mL/min flow rate.

to a log-normal distribution, with all of the conduit diameters concentrated below 1 mm. At the flow rate of 0.20 mL/min, the diameters of all conduits are mostly about 0.6 mm, which is larger than the other two flow rates. This also explains why the color of the wormhole is brighter at the 0.20 mL/min flow rate in Fig. 5. Although there are no potential ability for wormholes and branches to expand outward to form complex geometric shapes at a lower flow rate (Cooper et al., 2023), they can fully connect with the pore network to form a more stable wormhole structure. This explains the reason that the simple wormholes with large diameter are generated at low flow rates.

For the results discussed above, the process of wormhole formation may be different at different flow rates, in order to reveal the mechanism, the transition region between wormhole and pore network needs to be further understood. We used a higher precision CT scan to characterize this relationship across scales.

#### 4.3. Cross-scale Characterization

The quality of the produced image from CT scan depends on several factors, including the specifics of the instruments used, the sample size, and composition. These factors dictate the image resolution, sharpness, and contrast. Optimization of these factors is crucial for improving the quality of the image (Elkhoury et al., 2019; Pak et al., 2023). Smaller sample size leads to better CT image qual-

ity and more accurate pore identification (Lin et al., 2024). In this experiment, we first zoom into the inside of the gypsum sample with a high-resolution nondestructive scan to characterize wormholes across scales and also protect the integrity of the sample (Zhang et al., 2020). As shown in Fig. 8 (far left schematic diagram), when X-rays pass through the sample to reach the scanning area, they can be affected by the matrix outside of that area, causing scattering and attenuation of the X-rays. This can be particularly sensitive in high-resolution scans where the signal from within the sample is amplified, making noise more noticeable. That means the noise in the zoomed-in images is bigger than that in the full field of view scan (Chun et al., 2004).

##### 4.3.1. 2D Cross-scale Characterization

In order to avoid the influence of noise, methods including median filtering and pixel dilation are used to obtain the binary image as shown in Fig. 8. Comparing the images before and after binarization, the result is quite ideal for removing noise. Fig. 8(a), (c) show the same section at different resolutions, using the bubble (a diameter of 0.4 mm) as the reference (red box). Fig. 8(b), (d) represent the section of the next frame, as shown in the red circle, the wormhole around the bubble disappears, indicating that the wormhole is entering the bubble at this location. This phenomenon is only observed in images with 3.43  $\mu\text{m}$  resolution over one order of magnitude, but it was not clear in low-precision image. This also provides basic information for next quantitative analysis of wormholes in 3D under high-precision scanning.

##### 4.3.2. 3D Cross-scale Characterization

For the 3D binary matrices, a 50000-voxel 3D filter, which had an equivalent diameter of 160  $\mu\text{m}$  and 2 mm length filter were chosen so that the isolated pores and air bubbles can be effectively eliminated, and the wormholes could be preserved. Additionally, the pore networks were also rendered using the same algorithm (without filter) (as shown in Fig. 9 (b)). The pore space is very irregular, but it is well connected. While a resolution of 3.43 microns is not available for pores smaller than a micron, it is sufficient for millimeter-scale wormholes and micrometer-scale pore connections. The logical matrix corresponding to wormholes is established and combined with the 3D binary matrix of pore networks, presenting the pore networks and wormholes simultaneously, and then the wormholes observed clearly through transparent pore networks, as shown in the Fig. 9 (c). The wormholes (red color) are randomly distributed in the pore networks and throughout the whole sample, reflecting the heterogeneity of the fluid flow. Moreover, wormholes and pore networks are closely

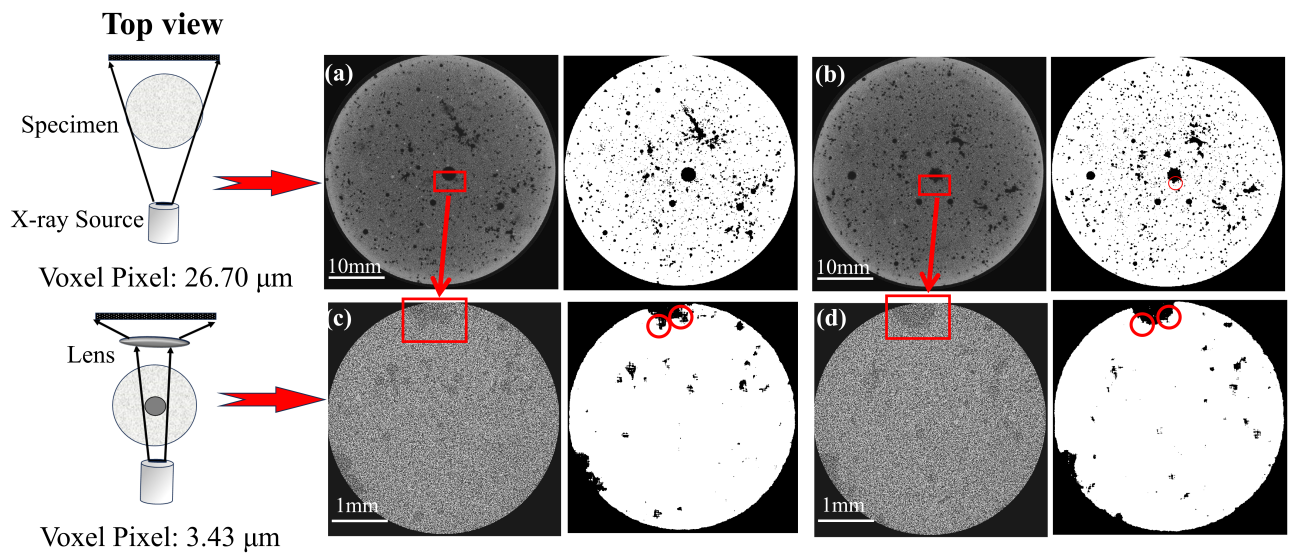


Fig. 8: Scanning methods and CT cross-section under low- and high-resolution: (a)(b): Continuous greyscale image at 26.70 micron-resolution; (c)(d): greyscale image at 3.43 micron-resolution; Red box indicates the same air bubble at the two resolutions; Red circle: Wormhole branches.

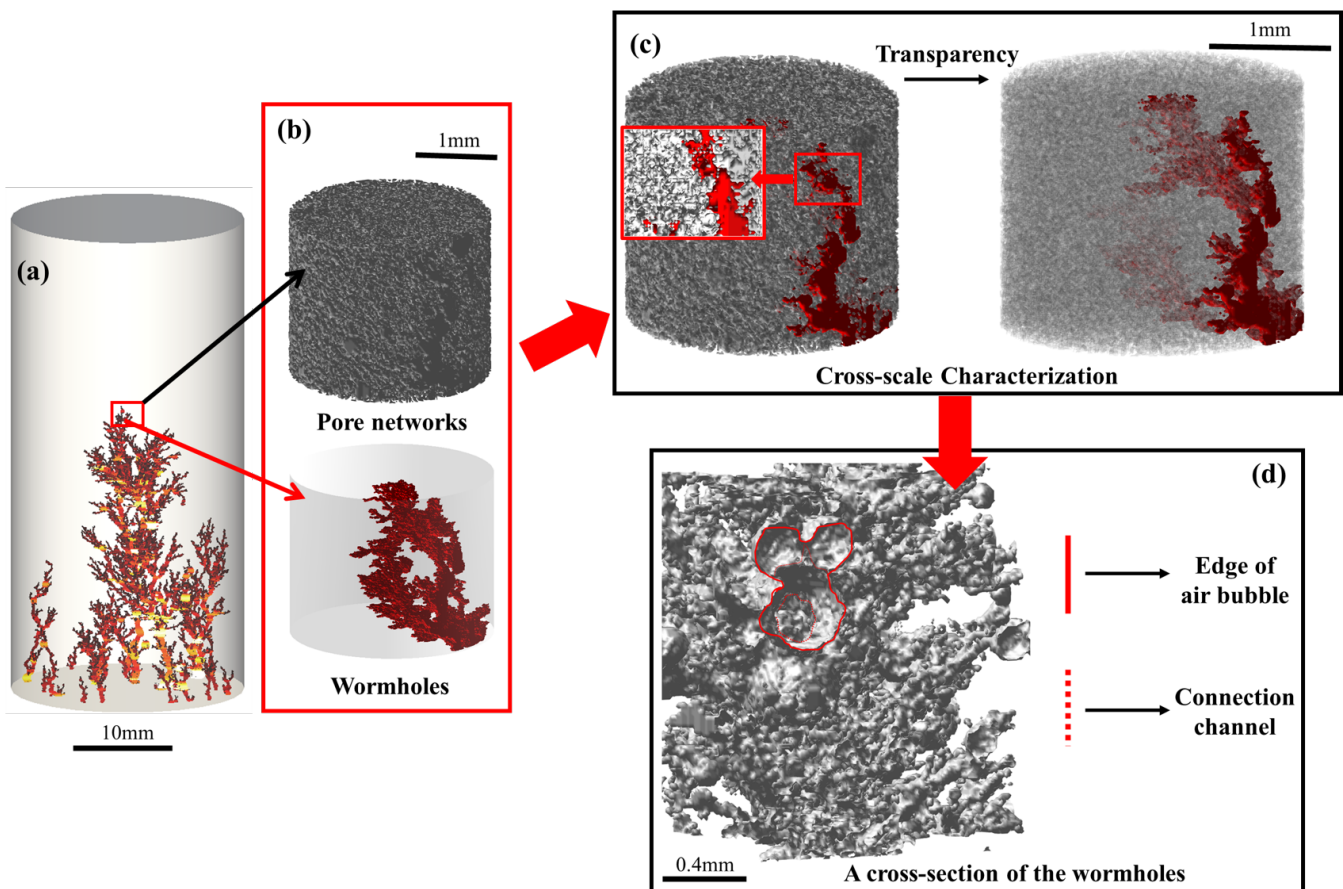


Fig. 9: Three dimensional reconstructions of the wormholes at low- and high resolution for sample G5 (1.80 mL/min).

connected and integrated and the 3D segmentation result of them makes it possible for us to quantitatively analyze their connections.

It is worth mentioning that by obtaining the vertical cross section of the wormhole, the connectivity between the punching hole and the bubble was observed (Fig. 9 (d)), which is impossible to rendering under low precision conditions. The fluid preferentially flows to the regions of highest permeability(Fredd and Fogler, 1998), and air bubbles can also be seen as the largest pores, voids, or natural fractures, reasonably explaining the stepped distribution of the curve in Fig. 6. Alas, due to limitations in hardware facilities (data increased tenfold), the diameter information of the wormhole at a resolution of 3.43 microns cannot be accurately obtained under high-precision conditions during rendering (see Fig. 9), potentially resulting in unsatisfactory imaging. However, this innovative analysis has already laid the foundation for our next quantification step.

## 5 CONCLUSION

In this study, we create wormholes in gypsum specimen using core flood tests. The wormholes resulting from different flow rates are observed using X-ray CT scan at two resolutions ( $26.70\text{ }\mu\text{m}$  and  $3.43\text{ }\mu\text{m}$ ). Topological and morphological algorithms are developed to process the 3D CT scan data, reconstructing and characterizing the geometry of wormholes and pore networks at two scales.

Initially, the area and quantities of conduits (wormholes and branches), especially the distribution of conduits diameters, are analyzed to provide quantitative descriptions of the complex wormholes and show how the flow rates affect the geometry of wormholes. More specifically, the total number of conduits at  $1.80\text{ mL/min}$  is about two or three times as many as those resulted from the other flow rates. The wormholes resulting from the flow rate of  $0.20\text{ mL/min}$  has a larger mean diameter ( $0.60\text{ mm}$ ) than those resulting from higher flow rates. The conduit diameter distribution represents the same trend at the  $0.20\text{ mL/min}$  and  $1.00\text{ mL/min}$  flow rate, respectively. Most importantly, using the non-destructive CT scanning method, 3D renderings of the wormholes and pore networks with different resolution are generated, enabling the two ideal 3D topologies presented simultaneously.

The cross-scale characterization provides us with a better understanding and theoretical basis for the relationship between wormhole formation and pore networks: 1) High-resolution scan with non-destructive method can generate unavoidable noise, which affects the image quality and makes quantification impossible; 2) The air bubbles with

micron scale will greatly affect the propagation and formation of wormholes; 3) Wormholes and pore networks connect and penetrate each other under high resolution image, making their boundaries indistinguishable. Next, we plan to modify the scanning method and cut the wormhole-pore network transition sub-sample from the inside of the specimen to minimize the noise of scanning as much as possible. This paper has laid the foundation for our next research direction.

## ACKNOWLEDGEMENT

We acknowledge the support from the Research Foundation for the State University of New York.

## REFERENCES

1. Andrew, M., Menke, H., Blunt, M. J., and Bijeljic, B. (2015). The imaging of dynamic multiphase fluid flow using synchrotron-based X-ray microtomography at reservoir conditions. *Transport in Porous Media*, 110(1):1–24.
2. Blunt, M. J., Bijeljic, B., Dong, H., Gharbi, O., Iglauer, S., Mostaghimi, P., Paluszny, A., and Pentland, C. (2013). Pore-scale imaging and modelling. *Advances in Water Resources*, 51:197–216.
3. Budek, A. and Szymczak, P. (2012). Network models of dissolution of porous media. *Physical Review E*, 86(5):056318.
4. Chun, I. K., Cho, M. H., Lee, S. C., Cho, M. H., and Lee, S. Y. (2004). X-ray micro-tomography system for small-animal imaging with zoom-in imaging capability. *Physics in Medicine & Biology*, 49(17):3889.
5. Cooper, M. P., Sharma, R. P., Magni, S., Blach, T. P., Radlinski, A. P., Drabik, K., Tengattini, A., and Szymczak, P. (2023). 4D tomography reveals a complex relationship between wormhole advancement and permeability variation in dissolving rocks. *Advances in Water Resources*, 175:104407.
6. Daccord, G. (1987). Chemical dissolution of a porous medium by a reactive fluid. *Physical Review Letters*, 58(5):479.
7. Daccord, G., Lenormand, R., and Lietard, O. (1993). Chemical dissolution of a porous medium by a reactive fluid-I. model for the “wormholing” phenomenon. *Chemical Engineering Science*, 48(1):169–178.
8. Deng, H., Fitts, J. P., and Peters, C. A. (2016). Quantifying fracture geometry with X-ray tomography: Technique of iterative local thresholding (TILT) for 3D image segmentation. *Computational Geosciences*, 20:231–244.
9. Einstein, H., Hirschfeld, R., Nelson, R., and Bruhn, R. (1969). Model studies of jointed-rock behavior. In *The 11th US Symposium on Rock Mechanics (USRMS)*. OnePetro.
10. Elkhoury, J. E., Shankar, R., and Ramakrishnan, T. (2019). Resolution and limitations of X-ray micro-CT with applications to sandstones and limestones. *Transport in Porous Media*, 129(1):413–425.
11. Fredd, C. N. and Fogler, H. S. (1998). Influence of transport and reaction on wormhole formation in porous media. *AICHe Journal*, 44(9):1933–1949.

12. Gouze, P. and Luquot, L. (2011). X-ray microtomography characterization of porosity, permeability and reactive surface changes during dissolution. *Journal of Contaminant Hydrology*, 120:45–55.
13. Gouze, P., Noiriel, C., Bruderer, C., Loggia, D., and Leprovost, R. (2003). X-ray tomography characterization of fracture surfaces during dissolution. *Geophysical Research Letters*, 30(5).
14. Grodzki, P. and Szymczak, P. (2019). Reactive-infiltration instability in radial geometry: From dissolution fingers to star patterns. *Physical Review E*, 100(3):033108.
15. Hoefner, M. and Fogler, H. S. (1988). Pore evolution and channel formation during flow and reaction in porous media. *AICHE Journal*, 34(1):45–54.
16. Johnson, K. S. (2008). Gypsum-karst problems in constructing dams in the USA. *Environmental Geology*, 53:945–950.
17. Li, W., Einstein, H., and Germaine, J. (2019a). Geometric and fractal analysis of complex wormholes resulting from gypsum core flood tests. In *ARMA US Rock Mechanics/Geomechanics Symposium*, pages ARMA–2019. ARMA.
18. Li, W. and Einstein, H. H. (2017). Theoretical and numerical investigation of the cavity evolution in gypsum rock. *Water Resources Research*, 53(11):9988–10001.
19. Li, W., Einstein, H. H., and Germaine, J. T. (2019b). An experimental study of matrix dissolution and wormhole formation using gypsum core flood tests: 1. Permeability evolution and wormhole geometry analysis. *Journal of Geophysical Research: Solid Earth*, 124(11):11055–11073.
20. Li, W., Germaine, J. T., and Einstein, H. H. (2022). A three-dimensional study of wormhole formation in a porous medium: Wormhole length scaling and a rankine ovoid model. *Water Resources Research*, 58(6):e2021WR030627.
21. Li, W. and Juanes, R. (2023). 3D image analysis of granular force chains. In *ARMA US Rock Mechanics/Geomechanics Symposium*, pages ARMA–2023. ARMA.
22. Lin, W., Chen, S., Li, X., Wang, Y., Zhang, Y., and Peng, Y. (2024). Quality enhancement of  $\mu$ -CT scanned shale images and optimization of experimental conditions. *Energy & Fuels*.
23. Lipar, M., Szymczak, P., White, S. Q., and Webb, J. A. (2021). Solution pipes and focused vertical water flow: Geomorphology and modelling. *Earth-Science Reviews*, 218:103635.
24. Menke, H. P., Bijeljic, B., Andrew, M. G., and Blunt, M. J. (2015). Dynamic three-dimensional pore-scale imaging of reaction in a carbonate at reservoir conditions. *Environmental Science & Technology*, 49(7):4407–4414.
25. Noiriel, C. (2015). Resolving time-dependent evolution of pore-scale structure, permeability and reactivity using X-ray microtomography. *Reviews in Mineralogy and Geochemistry*, 80(1):247–285.
26. Pak, T., Archilha, N. L., Berg, S., and Butler, I. B. (2023). Design considerations for dynamic fluid flow in porous media experiments using X-ray computed micro tomography—a review. *Tomography of Materials and Structures*, page 100017.
27. Serafeimidis, K. and Anagnostou, G. (2013). On the time-development of sulphate hydration in anhydritic swelling rocks. *Rock Mechanics and Rock Engineering*, 46(3):619–634.
28. Smith, M., Hao, Y., and Carroll, S. (2017). Development and calibration of a reactive transport model for carbonate reservoir porosity and permeability changes based on CO<sub>2</sub> core-flood experiments. *International Journal of Greenhouse Gas Control*, 57:73–88.
29. Smith, M. M., Sholokhova, Y., Hao, Y., and Carroll, S. A. (2013). CO<sub>2</sub>-induced dissolution of low permeability carbonates. part I: Characterization and experiments. *Advances in Water Resources*, 62:370–387.
30. Szymczak, P. and Ladd, A. (2009). Wormhole formation in dissolving fractures. *Journal of Geophysical Research: Solid Earth*, 114(B6).
31. Wang, H., Bernabé, Y., Mok, U., and Evans, B. (2016). Localized reactive flow in carbonate rocks: Core-flood experiments and network simulations. *Journal of Geophysical Research: Solid Earth*, 121(11):7965–7983.
32. Yang, Y., Hakim, S., Bruns, S., Rogowska, M., Boehnert, S., Hammel, J., Stipp, S., and Sørensen, H. (2018). Direct observation of coupled geochemical and geomechanical impacts on chalk microstructure evolution under elevated CO<sub>2</sub> pressure. *ACS Earth and Space Chemistry*, 2(6):618–633.
33. Zhang, Y., Niu, S., Du, Z., Hao, J., and Yang, J. (2020). Dynamic fracture evolution of tight sandstone under uniaxial compression in high resolution 3D X-ray microscopy. *Journal of Petroleum Science and Engineering*, 195:107585.